ACS OMEGA

http://pubs.acs.org/journal/acsodf

Article

Ab Initio Study of Hydrostable Metal−Organic Frameworks for Postsynthetic Modification and Tuning toward Practical Applications

Uchenna A. Anene* and S. Pamir Alpay

Cite This: *ACS Omega* 2022, 7, 7791−7805

Read Online

ACCESS | Metrics & More | Article Recommendations | Supporting Information

ABSTRACT: Metal−organic frameworks (MOFs), a subclass of nanoporous coordination polymers, have emerged as one of the most promising next-generation materials. The postsynthetic modification method, a strategy that provides tunability and control of these materials, plays an important role in enhancing its properties and functionalities. However, knowing adjustments which leads to a desired structure−function a priori remains a challenge. In this comprehensive study, the intermolecular interactions between 21 industrially important gases and a hydrostable STAM-17-OEt MOF were investigated using density functional theory. Substitutions on its 5-ethoxy isophthalate linker included two classes of chemical groups, electron-donating ($-NH_2$, $-OH$, and $-CH_3$) and electron-withdrawing ($-CN$, $-COOH$, and $-F$), as well as the effect of mono-, di-, and tri-substitutions. This resulted in 651 unique MOF−gas complexes. The adsorption energies at the ground state and room temperature, bond lengths, adsorption geometry, natural bond orbital analysis of the electric structure, HOMO−LUMO interactions, and the predicted zwitterionic properties are presented and discussed. This study provides a viable strategy for the functionalization, which leads to the strongest affinity for each gas, an insight into the role of different chemical groups in adsorbing various gas molecules, and identifies synthetic routes for moderating the gas adsorption capacity and reducing water adsorption. Recommendations for various applications are discussed. A custom Python script to assess and visualize the hypothetical separation of two equal gas mixtures of interest is provided. The methodology presented here provides new opportunities to expand the chemical space and physical properties of STAM-17-OEt and advances the development of other hydrostable MOFs.

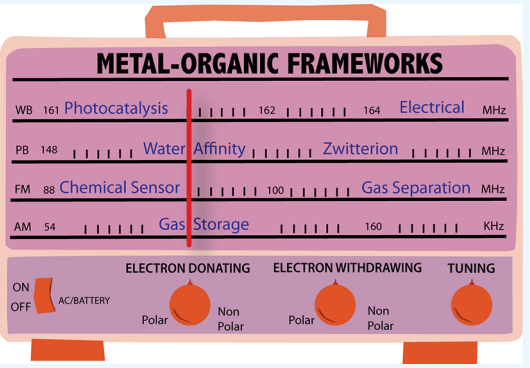

INTRODUCTION

The desire for technological breakthroughs and materials with advanced functionality has fueled the demand for novel materials. Among them are metal−organic frameworks (MOFs), porous crystalline polymers that have emerged as a promising next-generation material. They are modular and composed of both organic and inorganic molecules that provide a multitude of combinatory possibilities. MOFs garner a great deal of attention, which is reflected by the continued upward trend of research articles published on the topic in the past 10 years. Their commercial implementation is accelerating. Applications include MOF-based natural gas storage for powering vehicles by BASF chemical company,[1−3] ION-X[3−5] sub-atmospheric dopant gas storage and delivery system by NuMat Technologies for ion implantation, and the hydrogen fuel tank-powered Mercedes-Benz F125[6] concept car. They have been studied for applications in electrocatalysis,[7,8] drug delivery,[9] thin-film devices,[10] and batteries.[11,12] Their interconnected metal−ligand structure provides an extraordinarily large internal surface area and pore volume, more so than their counterparts: activated carbons,[13,14] zeolites,[15,16] and silica.[17,18] The pore sizes can range from ∼1 to 10 nm,[13] which makes them suitable for holding guest molecules of different sizes. With growing global environmental concerns[19] arising from industrial processes releasing carbon dioxide,[20−22] nitrogen dioxide, and sulfur dioxide,[23−25] MOFs are being studied as transformative[26] candidates for gas separation[27−29] and hydrogen[30,31] and methane[32] gas storage technologies.

Postsynthetic modification strategies allow MOF constructs to be altered with different reagents after the synthesis of the main structure; both the metal ions and/or organic linkers can be exchanged, allowing the opportunity to tailor the pore structure and size.[33] This approach provides tunability and control of MOFs' chemical and physical properties and has been key in expanding its design flexibility.[34−36] Aside from the experimental investigations on MOFs, first-principles calculations have been used extensively to probe the capabilities of

Received: November 24, 2021
Accepted: January 31, 2022
Published: February 16, 2022

MOFs and enhance their adsorption properties by ligand functionalization[37,38] or metal substitution.[39,40] However, despite the abundance of experimental and theoretical studies, designing and synthesizing materials with the desired structure−function a priori remains a challenge. A detailed investigation of the relative stabilities of adsorbed gas molecules on MOFs can provide the knowledge needed for tailoring the desired adsorption capacity and selectivity. Thus, quantum mechanical analysis using density functional theory (DFT) can help understand interactions that are difficult to observe through experiments.

Other factors that need consideration, especially for commercial applications, are the cost of the material and stability. One area that has received less research focus and is difficult to study experimentally is water stability. MOFs are moisture sensitive and are unstable at high humidity.

Though there are many excellent reviews and fundamental studies that show how a wide range of properties can be achieved by modifying the framework,[41−44] the impact that linker and/or metal substitution has on water adsorption has not been fully addressed. As the MOF is modified to increase gas adsorption and selectivity, it is likely to increase its affinity toward water. In addition, metal−ion exchange is known to enhance MOF's gas adsorption properties;[6] however, this could influence the stability of the MOF. For example, MOF-5 (IRMOF-1) has a tetrahedral arrangement[13] and has been considered for various applications.[45] Yet, MOFs that have only Zn^{2+} tetrahedral arrangements are known to be chemically unstable.[46,47] A material that has high gas adsorption capacity or selectivity cannot have commercial applications if it is unstable in humid environments or is too expensive to produce. The knowledge of the adsorption energy of the MOF with H_2O is crucial and thus considered as a reference point in this study. We aim to provide here a more comprehensive analysis to demonstrate the importance stability has on the final structure.

This study focused on a copper-based MOF, $Cu(C_{10}O_5H_8)\cdot 1.6H_2O$, called St. Andrews Material (STAM-17-OEt), in which Cu^{2+} is the central cation and the linker comprises a 5-ethoxy isophthalate moiety.[48] STAM-17-OEt is the ideal MOF for this study because there are three available positions on the linker for functionalization and it an open-metal site MOF, which is known for high adsorption properties.[49−51] More importantly, it was reported that poor hydrostability issues, which have plagued previous MOFs, have been resolved.[48] McHugh et al. demonstrated that STAM-17-OEt MOF retained its structure even after exposure to water for 1 year.[48] The electronic properties of STAM-17-OEt have not been fully investigated; this is done for the first time in this study. We also focus on the modification of the STAM-17-OEt linker using molecular DFT calculations to facilitate the design strategies and its advancement for gas adsorption and separation applications.

RESULTS AND DISCUSSION

Applying the computational details described in the Methodology section, the binding energies of 21 gas molecules on the original and functionalized STAM-17-OEt MOFs were calculated. Mono-, di-, and tri-substitutions on its 5-ethoxy isophthalate linker were considered, resulting in 651 different MOF−gas systems. The most important findings are summarized here, and the full results are provided in the accompanying Supporting Information, Table S1.

STAM-17-OEt Structure. The optimized structure parameters of STAM-17-OEt have not been reported in previous literature. Table 1 and Figure 1 show the calculated bond lengths of STAM-17-OEt after optimization. The computed bond lengths compare well with the values obtained from the powder X-ray diffraction (PXRD) experiment, with a deviation of ∼0.1 Å or less. These results suggest that using an LC-ωPBE exchange functional with cc-pVDZ and 6-311G(d, p) basis sets is reliable.

Table 1. Computed Bond Lengths of the Optimized STAM-17-OEt Compared to Bond Lengths Obtained from PXRD

	bond length (Å)	
DFT method	Cu−Cu	Cu−O
LC-ω-PBE/6-311G(d,p)/cc-pVDZ	2.70	2.00 (2)/2.02 (2)
		1.96 (2)/1.99 (2)
experiment[48,52]	2.57	1.87 (2)/2.04 (2)
		1.98 (2)/2.00 (2)

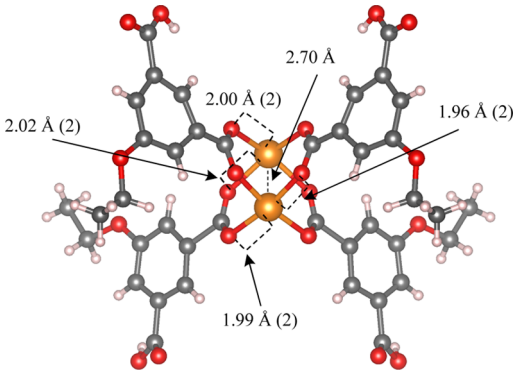

Figure 1. Optimized geometry of STAM-17-OEt.

Adsorption Energies of Gas Molecules on STAM-17-OEt. At the time of writing, a study of the adsorption capabilities of STAM-17-OEt over a range of gas molecules has not been reported. Therefore, to evaluate the performance of STAM-17-OEt for gas adsorption, 21 various gas molecules were adsorbed on the Cu center of the MOF. The choice of guest molecules are ones commonly found in industrial processes. Not only does this arrangement fully exploit the MOF possibilities, but the adsorption of these gases on the unmodified STAM-17-OEt also serves as a reference for comparison of the interactions after linker functionalization.

The adsorption energies ΔE_{ads} of the various gas molecules considered in this study (C_2H_2, C_2H_4, C_2H_6, C_3H_6, C_3H_8, C_4H_4S, C_6H_6, CH_4, Cl_2, CO, CO_2, H_2, H_2O, H_2S, H_2Se, HCN, N_2, NH_3, NO_2, O_2, and SO_2) are summarized in Figure 2 and Table 2. Negative energies and enthalpies correspond to an exothermic adsorption interaction. The larger negative value of binding energy indicates a more stable complex. There is diversity and a magnitude of differences between energies. By comparing the top five and bottom five adsorption energies, it follows this trend: $NH_3 \gg C_3H_6 >$ HCN > $H_2O > H_2S$ have the strongest binding energies (−91.0, −69.3, −69.0, −65.0, and −60.2, respectively), while $NO_2 \ll C_2H_6 < C_3H_8 < CH_4 <$ CO gases have relatively weaker binding energies (117.6, −9.4, −10.4, −11.6, and −12.6, respectively). It is not surprising that the strongest adsorption energy is seen with NH_3. HKUST-1, another MOF with a similar structure, is used for NH_3

https://doi.org/10.1021/acsomega.1c06658
ACS Omega 2022, 7, 7791−7805

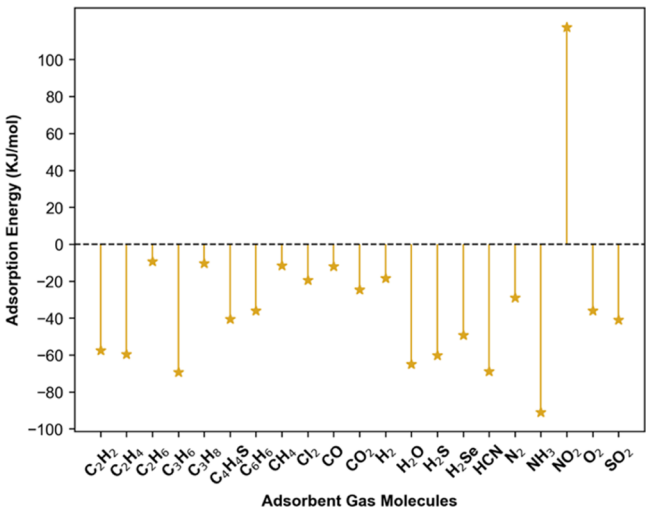

Figure 2. Calculated adsorption energies of 21 gases and the original unmodified STAM-17-OEt MOF.

Table 2. Calculated ΔE_{ads} (0 K) and ΔH_{ads} (298 K) on STAM-17-OEt Obtained from DFT calculations

	adsorption energy (kJ/mol)	
gas molecule	ΔE_{ads}	ΔH_{ads}
C_2H_2	−57.45	−51.30
C_2H_4	−59.57	−48.73
C_2H_6	−9.37	−3.26
C_3H_6	−69.31	−51.77
C_3H_8	−10.41	−4.71
C_4H_4S	−40.66	−33.96
C_6H_6	−36.10	−29.61
CH_4	−11.59	−4.49
Cl_2	−19.54	−14.97
CO	−12.10	−7.43
CO_2	−24.7	−19.31
H_2	−18.37	−3.57
H_2O	−65.04	−50.10
H_2S	−60.18	−48.15
H_2Se	−49.31	−38.44
HCN	−69.00	−61.72
N_2	−29.02	−22.03
NH_3	−90.96	−73.78
NO_2	117.56	127.51
O_2	−36.03	−29.31
SO_2	−41.06	−33.41

removal,[53,54] and STAM-17-OEt was reported to have a high uptake of NH_3 in an experiment.[48] All the adsorption energies are negative except for NO_2, meaning that the interaction between the Cu surface and NO_2 is repulsive and there is no adsorption.

Zero Point and Thermal Energy Contributions. Due to the simplicity of the model, it is not meaningful to directly compare calculated ΔE_{ads} to experimental data. However, by including zero-point vibrational energy and thermal energy correction calculations, enthalpies of adsorption ΔH_{ads} can be compared to experimental adsorption energies. The calculated ΔH_{ads} are presented in Table 2. The predicted ΔH_{ads} for CO_2 on a STAM-17-OEt of −19.3 kJ/mol is in reasonable agreement with an experimental isosteric heat of adsorption of −16.2 kJ/mol and at a higher pressure of −27.6 kJ/mol.[55] In the absence of additional experimental data, a definitive conclusion could not be reached for the other gases. However, the calculated ΔH_{ads} still gives us a sense of how STAM-17-OEt will perform under experimental conditions at 298 K.

Gas molecules typically interact on metal surfaces by one of the two possible adsorption mechanisms. The first is physisorption and it is the weakest interaction. The magnitude of the interactions ΔH_{ads} the range between −10.0 and −20.0 kJ/mol and is dominated by van-der-Waals forces.[56] The second is chemisorption; it is the strongest interaction and the gas undergoes a covalent chemical reaction. The ΔH_{ads} ranges between −80.0 and −500.0 kJ/mol.[56]

The results suggest that almost all of the gases ΔH_{ads} except for NO_2, which is noninteracting, fall within the physisorption range of −3.3 to −61.8 kJ/mol. With the understanding gained from the DFT functional benchmark analysis, the LC-ωPBE functional somewhat underestimates ΔH_{ads}; therefore, it is possible that NH_2 ΔH_{ads} of −73.8 kJ/mol may be in the chemisorption region.

Ligand-Functionalized STAM-17-OEt. In this investigation, two categories of functional groups were considered, electron-donating groups (−NH_2, −OH, and −CH_3), and electron-withdrawing groups (−CN, −COOH, and −F), as well as mono-, di-, and tri-substitutions of those groups. The functional groups above are listed in the order of their strength. The different classes of functional groups are meant to provide a general strategy to vary the degrees of electronegativity, which can then be elaborated to tune electronics and steric of the MOF for maximizing adsorption of a molecule, controlling gas selectivity, and adjusting the adsorption strength to the desired range. The results for the functionalization that yields the highest adsorption energy are summarized in Figure 3.

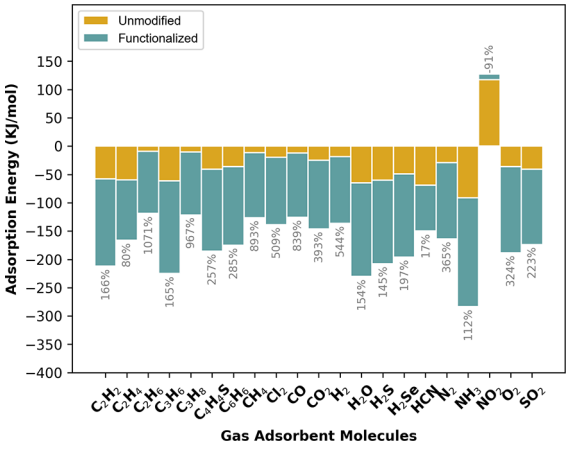

Figure 3. Comparison of adsorption energies for the 21 gas molecules on STAM-17-OEt for the most favorable substituted position compared to the unmodified. The green bar graph represents the magnitude of the increase in adsorption energies for the unmodified vs functionalized CN−$R_{2,4,6}$ (for HCN gas adsorption) and NH_2−R_2 (all the other remaining gases).

By taking the original unmodified STAM-17-OEt as a reference, Figure 3 and Table 3 show that the introduction of functional groups on the linker can significantly improve the adsorption capabilities of STAM-17-OEt. The mono-ortho substitution of the linker with NH_2 (NH_2−R_2) produced the greatest effect for all of the gasses except for HCN, which benefited from CN tri-substitution (CN−$R_{2,4,6}$). C_2H_6

https://doi.org/10.1021/acsomega.1c06658
ACS Omega 2022, 7, 7791−7805

Table 3. ΔH_{ads} (298 K) on Functionalized STAM-17-OEt Obtained from DFT Calculations

gas molecule	linker substitution	functionalized ΔH_{ads} (kJ/mol)
C_2H_2	NH_2-R_2	−146.12
C_2H_4	NH_2-R_2	−92.85
C_2H_6	NH_2-R_2	−102.01
C_3H_6	NH_2-R_2	−152.38
C_3H_8	NH_2-R_2	−103.89
C_4H_4S	NH_2-R_2	−136.65
C_6H_6	NH_2-R_2	−130.75
CH_4	NH_2-R_2	−106.45
Cl_2	NH_2-R_2	−112.84
CO	NH_2-R_2	−107.26
CO_2	NH_2-R_2	−114.98
H_2	NH_2-R_2	−102.35
H_2O	NH_2-R_2	−150.25
H_2S	NH_2-R_2	−134.22
H_2Se	NH_2-R_2	−134.21
HCN	$CN-R_{2,4,6}$	−72.06
N_2	NH_2-R_2	−126.33
NH_3	NH_2-R_2	−173.90
NO_2	NH_2-R_2	21.88
O_2	NH_2-R_2	−144.38
SO_2	NH_2-R_2	−123.63

improved the most from functionalization, increasing its original adsorption by 10 times from −9.4 to −109.7 kJ/mol. It is not surprising that STAM-17-OEt has a strong preference for NH_2 functionalization. Previous experimental studies reported that amine-functionalized MOFs facilitated the increased adsorption capacity,[57] separation performance,[58] and catalytic capacity in a DFT and experimental study.[59]

The other NH_2 substituted positions on the 5-ethoxy isophthalate linker showed moderate and sometimes decreased adsorption capacity in comparison to the unmodified MOF. Di-ortho-substituted ($R_{4,6}$) linker decreased adsorption for H_2 from −18.4 to −9.4 kJ/mol but showed moderate improvement for mono- and tri-substitution (R_6, $R_{2,6}$, and $R_{2,4,6}$) at −19.9, −19.2, and 20.2 kJ/mol, respectively. Most notably, C_2H_4, C_2H_6, CH_4, CO, and H_2S showed a ∼20% reduction or more in adsorption energy compared to the unmodified MOF. Their ΔE_{ads} is as follows: 1.12 kJ/mol ($R_{4,6}$) and −9.4 kJ/mol ($R_{2,4,6}$); −4.0 kJ/mol ($R_{4,6}$); −4.2 kJ/mol ($R_{4,6}$); −7.1 kJ/mol ($R_{4,6}$); and −45.8 ($R_{2,4,6}$), respectively. This suggests that the substituted positions may be used to influence and fine-tune adsorption capacity and selectivity. This concept is explored in more detail in the next section.

What is interesting is that the amino ortho-substitution (NH_2-R_2) of the linker could result in a novel zwitterion intermediate. Zwitterions are neutral compounds that contain both positively and negatively charged functional groups. What structure predominates depends on the pH. At neutral pH, STAM-17-OEt could exist as a zwitterion, where the amino group is protonated to yield ammonium ($-NH_3^+$) and the carboxyl is deprotonated to yield a carboxylate anion (COO^-). In an acidic solution, both the amino and carboxylate functional groups are protonated to form $-NH_3^+$ and −COOH. In a basic solution, they both are deprotonated to yield $-NH_2$ and $-COO^-$. These substituent properties open the door for additional strategies to control the MOF functionality with pH. Ionic MOFs offer an additional opportunity for gas selectivity.[60]

Linker functionalization made the interaction of NO_2 on the surface energetically more favorable from 117.6 to 10.0 kJ/mol; however, it remained repulsive. This could be due to the structural degradation of the MOF. The capture of acidic gases such as NO_2, SO_2, and CO_2 is challenging due to their highly corrosive and oxidizing nature. In particular, NO_2 is known to react and degrade MOF materials. Copper-based HKUST-1 MOF is unstable in NO_2 conditions. After NO_2 adsorption, the gas reacts with the copper node and forms copper nitrate [$Cu(NO_3)_2$], causing the MOF crystalline structure to collapse and reduce the adsorption capacity.[61,62]

All the thermodynamic quantities are not reported in Table 3 for the other functional groups and gases; however, they have been calculated. The DFT raw data output files to determine additional ΔE_{ads} (298 K) and ΔH_{ads} (298 K) with eqs 2 and 3,

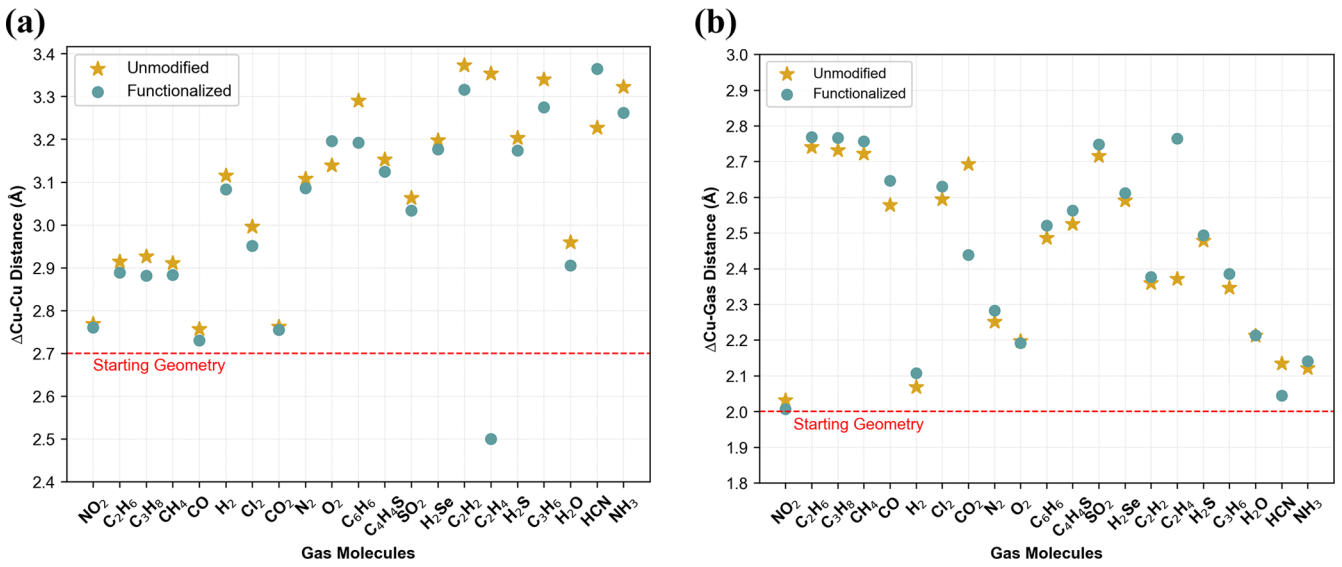

Figure 4. (a) Cu−Cu distance and (b) Cu−gas distance after gas adsorption. The starting geometry refers to the Cu−Cu distance and the Cu−gas distance before adsorption. Adsorbed gas ΔE_{ads} of the unmodified MOF are listed in an increasing order on the *x*-axis.

https://doi.org/10.1021/acsomega.1c06658
ACS Omega 2022, 7, 7791−7805

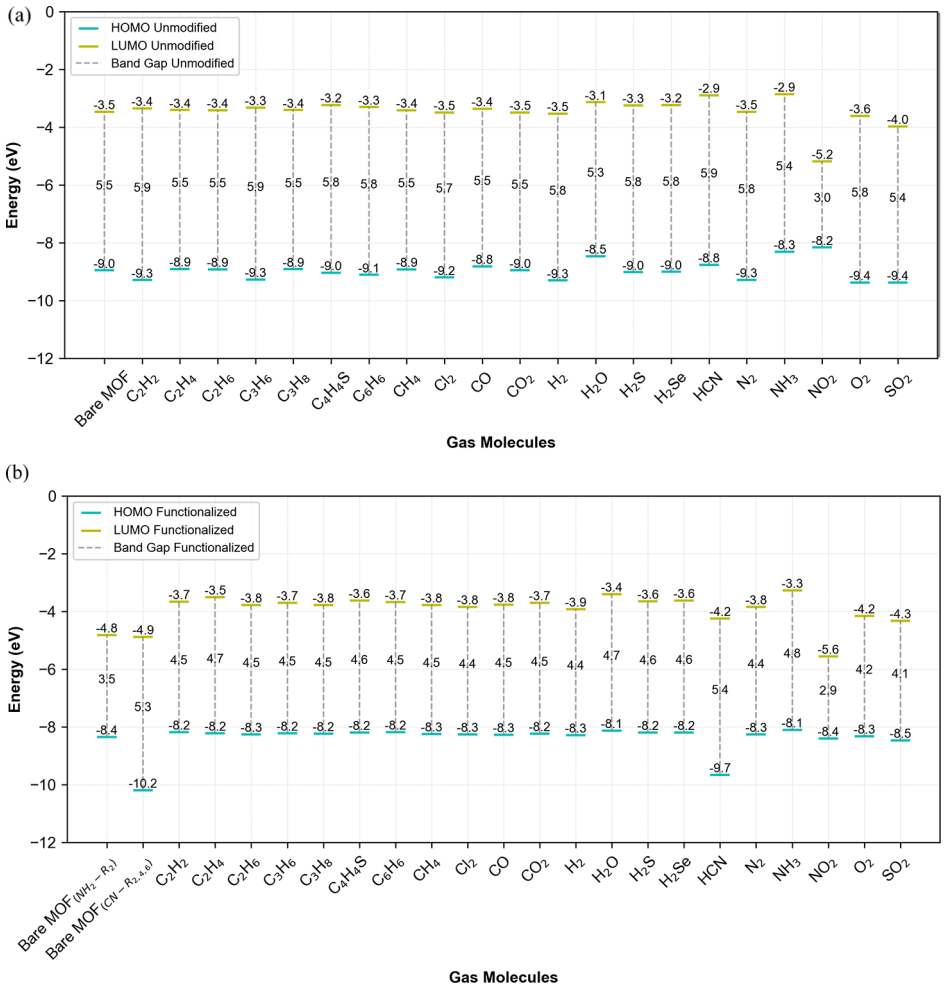

Figure 5. Values of the HOMO and LUMO energies and their band gaps of the bare MOF structure and MOF + gas complexes (a) Unmodified STAM-17-OEt MOF. (b) Functionalized STAM-17-OEt MOF.

respectively, are publicly available on the NoMaD Repository.[63]

Gas Adsorption Configurations of Unmodified and Functionalized MOF. Adsorption geometry and stability of gas molecules on metal surfaces can be key parameters for determining the properties, functions, and adsorption strengths of MOFs. The MOF structure can be flexible or rigid. The flexible MOFs exhibit reversible adsorption−desorption structural transformations that are classified as "breathing."[64,65] There is shrinkage or expansion of the unit cell volume and shortening or elongation of the distance between the metal node and linkers or twisting mechanisms.[64−66] This mechanical behavior makes these particular types of MOFs enticing for use as stimulus-responsive MOFs,[67] such as chemical sensors to diagnose diseases such as diabetes[68] or detect toxic gases.[69] The following results suggest that STAM-17-OEt exhibits expansion and contraction in the structure for certain gas molecules that are indicative of the motion present in some breathing MOFs.

The effect of adsorbing different gases on the unmodified and functionalized STAM-17-OEt is illustrated in Figure S1. These are the configurations that correspond to the adsorption energies presented in Tables 2 and 3. All the gas molecules had the same starting geometry and distance from the Cu surface, as shown in the Methodology section. The gas molecules adopt a unique geometry when adsorbed on the Cu surface. The unsaturated bonds of C_2H_2 and C_2H_4 are parallel to the Cu surface before and after the MOF is functionalized. CO_2 has a bidentate adsorption geometry, parallel to the surface, but tilts slightly after functionalization. Surprisingly, C_2H_4, C_2H_6, CH_4, N_2, NH_3, and NO_2 adsorption geometries remained unchanged, even though their adsorption energies doubled after functionalization. The HCN structure also remained relatively unchanged although it only showed a 17% improvement in adsorption energy after functionalization. Therefore, the relationship between the adsorption geometry and energies is inconclusive.

To better visualize the structural transformation in a STAM-17-OEt paddle-wheel structure, the Cu−Cu and Cu−gas distances for the unmodified and functionalized MOF are plotted in Figure 4a,b and the values are reported in Table S2. The gas molecules are ordered from the lowest to the highest adsorption energy on the *x*-axis. The bond distances vary between the different MOF−gas complexes. The binding strength appears to be independent of the Cu−Cu distance. For most of the gases, upon adsorption, the Cu−Cu bond distance widened, going from a starting geometry of 2.7 Å to as wide as 3.37 Å for the unmodified MOF (C_2H_2) and 3.36 Å after functionalization (HCN). C_2H_4 was the only gas that dropped to 2.5 Å after modification.

Similarly, for the Cu−gas complex, the adsorption strength appears to be independent of the distance. NO_2, which was

https://doi.org/10.1021/acsomega.1c06658
ACS Omega 2022, 7, 7791−7805

noninteracting, and NH_3, with the highest adsorption energy, have the shortest average Cu−gas distances at 2.03/2.01 Å and 2.12/2.14 Å, for the unmodified and functionalized MOF, respectively. However, saturated hydrocarbons did show some similarities. C_2H_4, C_2H_6, and CH_4 have equivalent Cu−gas distances and the same trend is observed for the Cu−Cu bond distance.

The adsorption of gases with various sizes and geometry has revealed STAM-17-OEt structural flexibility and the ability to adapt to different gases through a range of different conformational changes. With many MOF applications requiring structural pliancy, STAM-17-OEt should be investigated further with periodic DFT calculations to explore its breathing behavior and quantify its mechanical properties. Most notably, C_2H_4, C_6H_6, and HCN, which exhibited large deformations upon gas adsorption in both the unmodified and functionalized MOF, may be good candidates for gas sensing.

HOMO−LUMO Energy Band Gap. To obtain a qualitative understanding of the influence of the adsorbed gas molecules and functionalization on the electric charge, the energy gap was analyzed. The HOMO and LUMO describe the ability to donate an electron and obtain an electron, respectively, and can help predict electronic stability and chemical reactivity of the MOF. In general, the introduction of an electron donor will increase the HOMO level and an electron acceptor to a conjugated molecule will lower LUMO levels. The values of the HOMO, LUMO, and their band gap energies of STAM-17-OEt are illustrated in Figure 5. Although DFT methods tend to underestimate band gaps, the results can still serve as a qualitative reference when comparing the MOF−gas complexes to bare MOFs. The HOMO and LUMO energy differences correspond to the conduction band valence energy level difference. The band gap ranges from 3.0 to 6.0 eV for unmodified MOFs and 2.9 to 5.4 eV for the functionalized MOF. The distance between the HOMO and LUMO increased upon adsorption of a gas molecule, relative to the bare MOF for both the unmodified and functionalized MOF. The plots for the other complexes are also very similar. Similar behavior was reported for MIL-53 MOFs, where the band gap was tuned with pressure, temperature, and guest−molecule interactions.[70] They are now being investigated for piezoelectric applications.

Furthermore, by functionalizing the STAM-17-OEt linker with amino or cyano functional groups the HOMO, LUMO, and band gap energies are reduced by 36% to 3.6 eV and 3% 5.3 eV, respectively. A narrower band gap increases the conductivity of the Cu relative to the bare and unmodified MOFs and a narrow band gap is necessary for photocatalytic applications. In addition, the electron densities of the HOMO and LUMO are visualized in Figure 6 (full analysis Figure S2). Looking at the HOMO of the unmodified MOF, before gas adsorption, the electron density is well localized on the C−O bond of the methoxy, while the LUMO is concentrated on the oxygen of the Cu−O bond of the linker. After adsorption of a gas molecule, both the LUMO and HOMO changed, indicating that the gas molecule was adsorbed on the Cu surface and a charge transfer occurred, supporting what was observed earlier with an increase in the band gap. In comparison, the HOMO of the functionalized MOF with CN, before gas adsorption, the electron density is well localized on the oxygen of the carboxylate and the LUMO is concentrated on the oxygen of the C−O bond of the linker. The HOMO of the functionalized MOF with NH_2, before gas

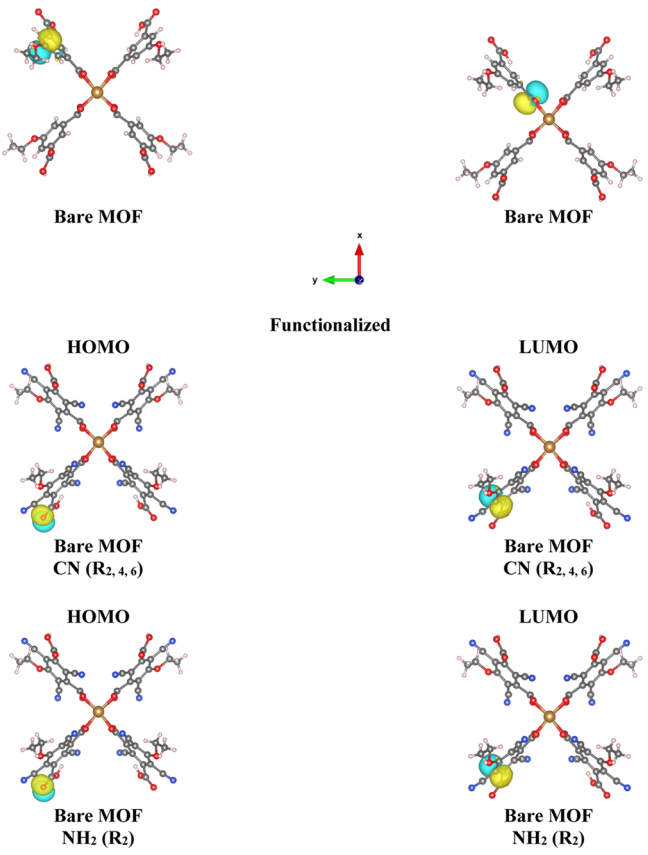

Figure 6. Isosurface of the HOMO and LUMO of the bare unmodified and amino (NH_2−R_2)- and cyano (HCN−$R_{2,4,6}$)-functionalized STAM-17-OEt. Isovalue was set to 0.04.

adsorption the electron density is well concentrated on the C−O bond of the methoxy and while the LUMO is concentrated on the oxygen of the Cu−O bond of the linker. After adsorption, both the LUMO and HOMO change corresponding to the different configurations observed in the earlier section.

Natural Bond Orbital Analysis. Natural bond orbital (NBO) analysis was carried out to gain further insights into the structure and guest molecule interactions that occur before and after amino (NH_2−R_2) and cyano (HCN−$R_{2,4,6}$) substitutions. The calculated natural atomic charges and the natural electron configuration for STAM-17-OEt were obtained from an NBO analysis. The analysis of the bare MOF and the MOF−gas complexes are reported in Table S3. The selected results that include the bare unmodified and functionalized MOFs and the MOF−gas complexes for the highest (NH_3) and lowest (NO_2) adsorbing gas molecules are reported in Table 4. The natural electron configurations of the two Cu atoms in the bare unmodified MOF are [core]-$4s^{(0.24)}3d^{(9.77)}4p^{(0.27)}4d^{(0.01)}$ and [core]-$4s^{(0.36)}3d^{(9.30)}4p^{(0.36)}4d^{(0.01)}6p^{(0.01)}$. The 0.01 electrons in 4d and 6p orbitals are relatively smaller than the other orbitals and make a negligible contribution and therefore are omitted from the discussion. The results show that the Cu^{2+}-ion coordination with oxygen is mainly on the 4s, 3d, and 4p orbitals. The calculated natural charges on the copper atom in the complex are (+0.7 e) and (+1.0 e); this is smaller than the idealized formal charge of +2, indicating a charge transfer from the donor atoms of the linker to the copper metal ion. The results reveal that one Cu atom is oxidized less than 1+ (+0.7 e) and

https://doi.org/10.1021/acsomega.1c06658
ACS Omega 2022, 7, 7791−7805

Table 4. Natural Atomic Charges and Natural Electron Configurations of Bare STAM-17-OEt MOF and MOF−Gas Complexes Obtained from Natural Bond Analysis

systems	atom	natural charge	natural electron configuration
bare MOF (unmodified)	Cu (1)	0.7	[core]4S(0.24)3d(9.77)4p(0.27) 4d(0.01)
	Cu (2)	1.0	[core]4S(0.36)3d(9.30)4p(0.36) 4d(0.01)6p(0.01)
	O (1)	−0.6	[core]2S(1.61)2p(4.99)3d(0.01)
	O (2)	−0.6	[core]2S(1.61)2p(4.99)3d(0.01)
	O (3)	−0.6	[core]2S(1.71)2p(4.87)
	O (4)	−0.6	[core]2S(1.71)2p(4.87)
	O (5)	−0.7	[core]2S(1.66)2p(4.98)3p(0.01)
	O (6)	−0.7	[core]2S(1.66)2p(4.98)3p(0.01)
	O (7)	−0.6	[core]2S(1.68)2p(4.90)3p(0.01)
	O (8)	−0.6	[core]2S(1.68)2p(4.90)3p(0.01)
	O (9)	−0.6	[core]2S(1.58)2p(4.98)3p(0.01) 3d(0.01)
	O (10)	−0.6	[core]2S(1.58)2p(4.98)3p(0.01) 3d(0.01)
	O (11)	−0.7	[core]2S(1.71)2p(4.95)3p(0.01)
	O (12)	−0.7	[core]2S(1.71)2p(4.95)3p(0.01)
	O (13)	−0.7	[core]2S(1.66)2p(5.00)3d(0.01)
	O (14)	−0.7	[core]2S(1.66)2p(5.00)3d(0.01)
	O (15)	−0.6	[core]2S(1.69)2p(4.85)3d(0.01)
	O (16)	−0.6	[core]2S(1.69)2p(4.85)3d(0.01)

(+1.0 e). These results are consistent with the HOMO−LUMO results in Figures 6 and S2, where the HOMO consists of π orbitals of the benzene ring and carbonyl and LUMO are composed of π orbitals of oxygen. The Cu dimer is complexed with very electronegative oxygen atoms and is most likely the major contributor to the charge transfer.

The natural electron configurations of Cu^{2+} ions in the bare amino-functionalized MOF (NH_2−R_2) are [core]-$4s^{(0.18)}3d^{(9.88)}4p^{(0.20)}$ and [core]$4s^{(0.33)}3d^{(9.41)}4p^{(0.36)}6p^{(0.01)}$. The calculated natural charge on the copper atom in the functionalized complex is (+0.7 e) and (+0.9 e). Again, the orbitals of all Cu atoms show a gain of electrons (less positive). However, there is a greater charge transfer from the functionalized ligand than the unmodified, presumably from the amino functional. Moreover, the results are further supported by Mulliken population analysis and Pipek−Mezey criteria, with the formal charges of the two Cu(II) complexes of (+0.4 e, +0.6 e) and (+0.4 e, +0.6 e) for the unmodified and (+0.4 e, +0.6 e) and (+0.4 e, +0.6 e) for the amino-substituted, respectively. The unmodified and functionalized MOF could be described as ligand-to-metal charge-transfer complexes, which show potential for photosynthetic applications.

The calculated natural charge and natural electron configurations for the bare unmodified and functionalized MOF and the MOF−gas complex of the highest (NH_3) and lowest (NO_2) adsorption energies are reported in Table 4. Looking at the bare unmodified MOF, the calculated natural charge of +0.7/+1.0 e on the Cu atoms is smaller than the formal charge Cu^{+2}. This value is expected because the MOF paddle wheel structure is a dimer and the charge is split between the two Cu atoms. In comparison to the NH_2- and CN-functionalized bare MOF, the calculated natural charges are +0.7/+0.9 e and +0.8/+1.1 e. Interestingly, one of the Cu atoms is more positive and less electron dense than the other Cu atom for the unmodified and CN-functionalized MOF. After adsorption, the charge analysis shows a net charge on the Cu atom in both the unmodified and functionalized MOF−NH_3 gas complexes. It indicates a reduction in electron density on the Cu atom and a more positive natural. The differences in partial charges after adsorption reveal the transfer from the Cu to the NH_3 gas molecules. In contrast, the electron density for both the unmodified and functionalized MOF−NH_3 gas complexes increased around the Cu and it becomes more negative. This indicated that there is a charge transfer from the NO_2 gas molecules to the Cu atoms. This could be the explanation as to why NO_2 is noninteracting and not adsorptive to the MOF.

Tuning Adsorption Strength and Selectivity by Ligand Functionalization. What was reported in the previous section were the functionalized positions and number of substitutions on the STAM-17-OEt linker needed to yield the strongest adsorption energies when compared to its unmodified structure. However, for some industrial applications, the strongest adsorption energy may not be ideal or more flexibility in the design is required for extreme conditions (e.g., elevated temperature and pressure). Sometimes this is overlooked in computational studies that evaluate MOFs for gas capture.

For example, postcombustion capture of CO_2 lies between physisorption and chemisorption, between the range of −25.0 to −40.0 kJ/mol.[71] Physisorption materials for the postcombustion capture of CO_2 can operate at temperatures above 200 °C and high-pressure environments, the low ΔH_{ads} reduces the energy cost required to regenerate CO_2.[72] For chemisorption, amine can be incorporated on the surface to increase the affinity of CO_2; however, this process can increase the amount of energy needed to desorb CO_2, and the material tends to degrade at temperatures above 120 °C.[71,72] To achieve more efficient processes, MOF material development should be tightly linked to minimizing the ΔH_{ads} while maximizing the adsorption capacity and providing the flexibility to accommodate different operating conditions. The strategy to include mono-, di-, tri-, and ortho/para substitutions in the study offers the opportunity to moderate MOF adsorption strength for the desired application.

It is clear from Figure 7 that an amino-functionalized STAM-17-OEt linker yields the highest adsorption energies,

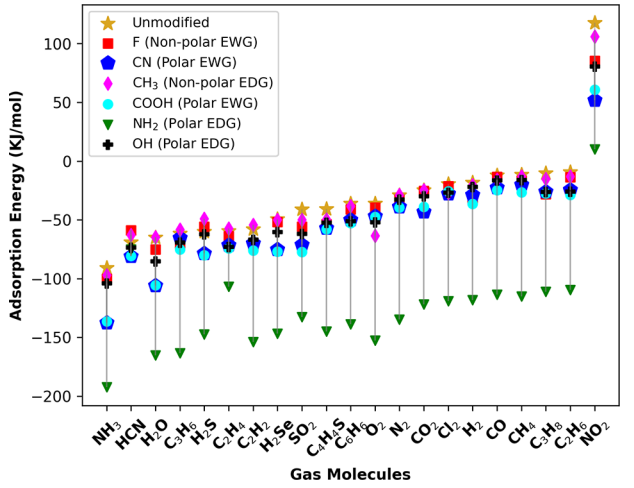

Figure 7. Comparison of the lowest adsorption energies for each functional group considered in this study.

https://doi.org/10.1021/acsomega.1c06658
ACS Omega 2022, 7, 7791−7805

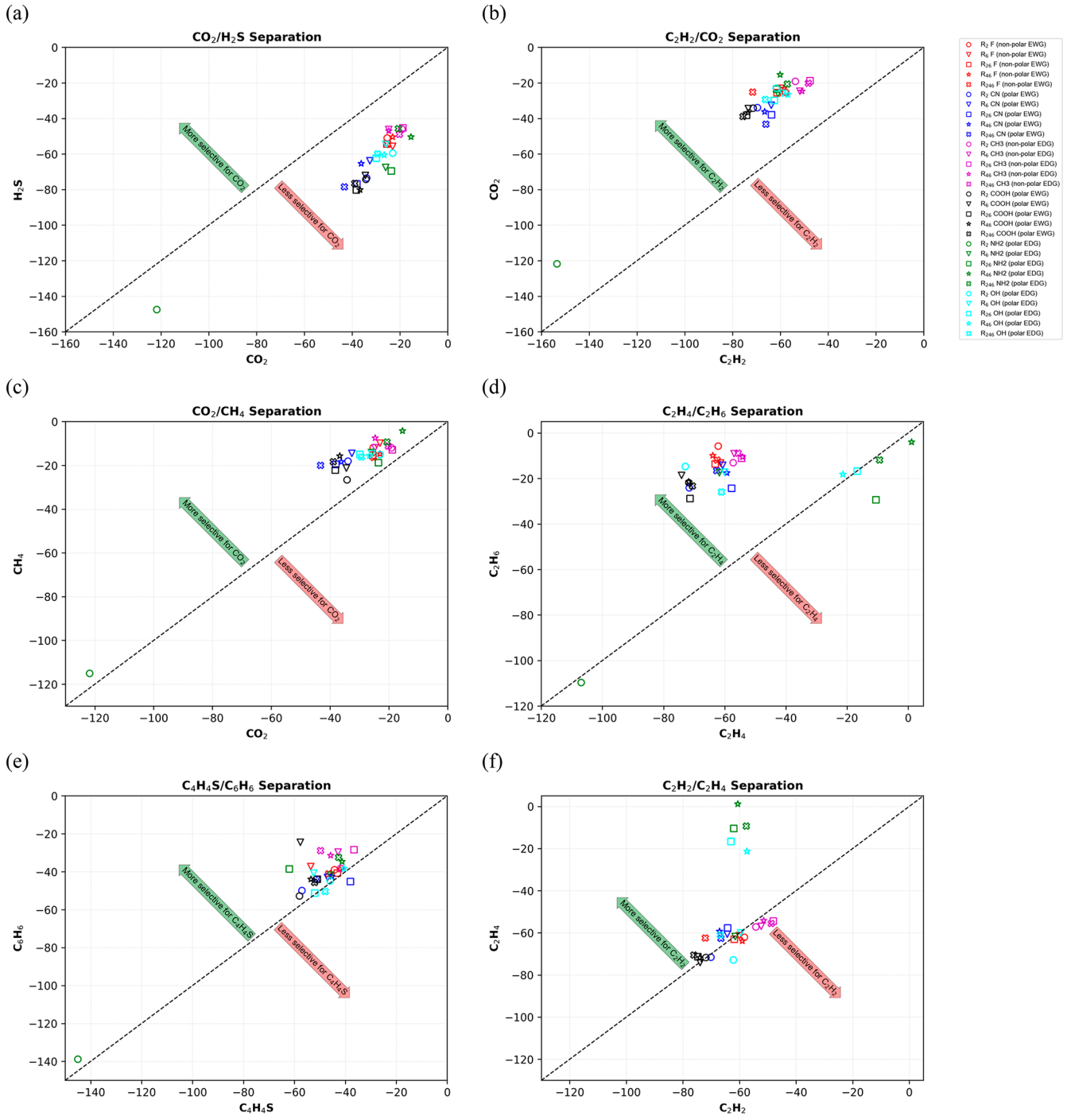

Figure 8. (a–f) Scatter plots of adsorption energies of two equal gas mixtures to illustrate the potential gas separation performance of STAM-17-OEt. Note: the dashed diagonal line is not a regression line; the line is independent of the data, and its purpose is to help visualize the two gas separations.

but for high-temperature or pressure environments that are known to increase adsorption putting the adsorption energy in the chemisorption range may not be the best option. Instead, using polar EWG CN or COOH can reduce the adsorption energy for most gases. For NH_3 gas adsorption, using a polar EWG reduces it by almost 50%. O_2 adsorption energy can best be reduced by using a non-polar EDG CH_3.

Tuning Gas Selectivity by Selecting the Substituted Position. Much of the work presented here has been fundamental and general, with a wide range of technological applications. However, for concreteness, this section will describe a specific application relating to gas selectivity. Selective adsorption can be achieved based on the difference in adsorption energy between the two gasses of interest. Tuning the affinity of STAM-17-OEt toward particular gas of interest is crucial for optimizing its adsorptive properties for commercial applications. Figure 8a–f illustrates idealized theoretical cases of an equal mixture of gas of two gases separated with STAM-17-OEt. Using the difference in adsorption energies of the two gases as a basis for selectivity, Figure 8a–c suggests that the MOF could separate H_2S from CO_2, C_2H_2 from CO_2, and CO_2 from CH_4. Figure 8a shows

https://doi.org/10.1021/acsomega.1c06658
ACS Omega 2022, 7, 7791−7805

that the best separation of H_2S/CO_2 can be obtained by using either a di- or tri-substitution with a polar EWG ($R_{2,6}$, $R_{4,6}$, $R_{2,4,6}$ COOH, or $R_{2,6}$, $R_{2,4,6}$ CN). Figure 8b, C_2H_2/CO_2 separation can best be obtained by using substitutes with a COOH polar EWG or with di-substitution with a NH_2 polar EDG ($R_{4,6}$ NH_2).

There are scenarios where the MOF's selectivity can be switched by using different functional groups or by regioselectivity. The resulting plots for C_2H_4/C_2H_6, C_6H_6/C_4H_4S, and C_2H_2/C_2H_4, are shown in Figure 8d–f. In Figure 8d, most of the functional groups can be used to make C_2H_4 more selective than C_2H_6, except for the ones that fall on the dotted line. However, a di-ortho substation with polar EDG NH_2 ($R_{2,6}$) can shift selectively to C_2H_6. C_2H_6 and C_2H_6 are very close in adsorption energies, but by selecting a mono-ortho COOH substitution, the MOF can be selective for C_4H_4S (R_6) or switch selectivity to C_6H_6 by selecting di-ortho CN ($R_{2,6}$) substitution. In a final example, the MOF could be made more selective for C_2H_2 with OH di- and tri-substitutions but could possibly be switched to C_2H_4 with mono-ortho OH substitution (R_2).

Additional illustrations on the possible selectivity and separation of two gases on this MOF material are displayed in Figure S3. The Python-based plotting script that was developed to easily separate and visualize the effect of the mono-, di-, and tri substitutions is available on the first author's GitHub. While these predictions can provide some useful information regarding the adsorption selectivity of a particular functionalized MOF, further investigations under real industrial conditions are still needed for its full assessment.

Functionalization for Stability in Moisture Environments. Although STAM-17-OEt is highly stable in water, the gas adsorption capacity and strength may be sensitive to water or humid environments. From the results in the earlier section, it is evident that water adsorbs more strongly than most of the gases. Other theoretical studies functionalize MOFs to improve adsorption without also considering the increase in the MOF's affinity for water. However, in real industrial applications, moisture could adversely affect the adsorption of gases. As it will be shown in the following, maintaining the balance of low water adsorption and high gas affinity is difficult.

Earlier, it was determined that amine- and cyano-functionalized MOFs enhanced gas adsorption for all gases including H_2O. To counteract this effect, the STAM-17-OEt linker could be functionalized with different strategies that could lower the water affinity while still increasing or maintaining gas adsorption capacity. In this section, three substitution strategies are investigated to demonstrate an approach to reduce water adsorption.

Strategy 1: functionalization of the linker with a different amino or cyano substitution patterns. In this strategy, tri-amino substitution (NH_3–$R_{2,4,6}$) for the 20 gases and cyano substitution (CN–$R_{2,4,6}$) for HCN gas yield lower H_2O adsorption energy. Strategy 2: functionalization of the linker with tri-methyl substitution (CH_3–$R_{2,4,6}$). For this strategy, this substitution pattern is the most unfavorable for H_2O and yields the lowest adsorption energy. Strategy 3: functionalization of the linker with a nonpolar functional group, while selecting the situation pattern that gives the highest gas adsorption. In this strategy, nonpolar functional groups yield low water adsorption and good gas adsorption energies.

The results are illustrated in Figure 9. The adsorption energies of the unmodified MOF and the predicted most

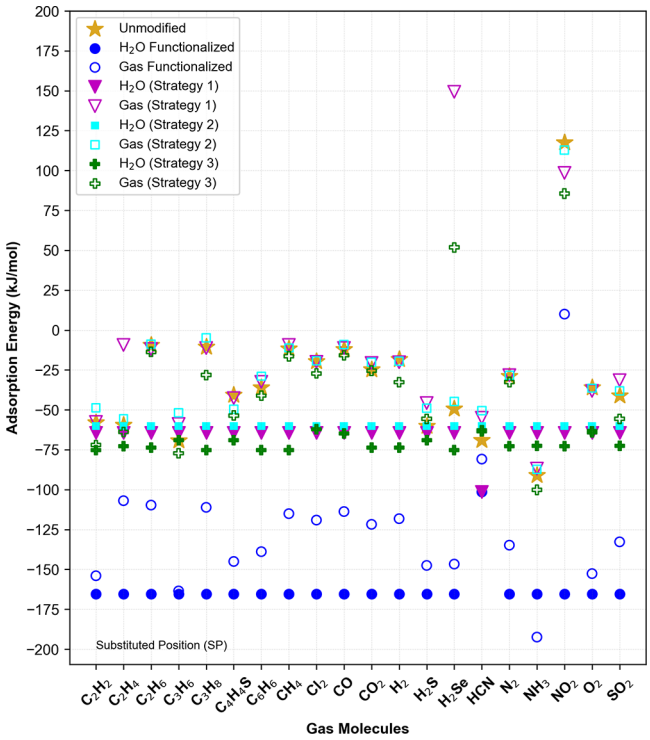

Figure 9. Three MOF functionalization strategies were tested to reduce the competitive adsorption of water to gas: Strategy 1, functionalization of the linker with a different amino or cyano substitution pattern. In this strategy, tri-amino substitution (NH_3–$R_{2,4,6}$) for the 20 gases and cyano substitution (CN–$R_{2,4,6}$) for the HCN gas. Strategy 2, functionalization of the linker with tri-methyl substitution (CH_3–$R_{2,4,6}$). Strategy 3, functionalization of the linker with a nonpolar functional group while selecting the substitution pattern that gives the highest gas adsorption. The unmodified (gold star) and the amine-functionalized (dark blue circle) MOF adsorption energies are included as references.

favorable positions, (NH_3–R_2) and (CN–$R_{2,4,6}$) are included as a reference. The filled plot markers indicate that H_2O is adsorbing more strongly than the gas molecules. If strategy 1 is applied, H_2O adsorption is reduced from −165.4 to −64.3 kJ/mol. HCN gas adsorption is unchanged because tri-cyano substitution also gives lower H_2O adsorption energy. Because amino substitution (NH_3–R_2) improved the adsorption energy of 20 gases and cyano substitution (CN–$R_{2,4,6}$) for the HCN gas, selecting a different substitution pattern on the linker would decrease water adsorption. However, strategy 1 still results in H_2O adsorbing more strongly than gas molecules. If strategy 2 is applied, tri-methyl substitution (CH_3–$R_{2,4,6}$) will give the lowest H_2O adsorption energy. This substitution pattern decreased H_2O adsorption energy from −165.4 and −101.4 to −60.1 kJ/mol. However, in strategy 2, the difference between the H_2O and gas adsorption energies remained relatively unchanged and H_2O still adsorbed more strongly than gas molecules. If strategy 3 is applied, the linker is functionalized with either a CH_3 or F nonpolar functional group because they yield lower H_2O adsorption. The choice of a nonpolar functional group was determined by the one that gave the highest gas adsorption. By applying strategy 3, tri-fluoro substitution (F–$R_{2,4,6}$) for the C_2H_2 gas, ortho-fluoro substitution (F–R_6) for the C_3H_6 gas, ortho-methyl substitution (CH_3–,R_6) for the HCN gas and di-fluoro substitution (CH_3–$R_{2,6}$) for the O_2 gas, their adsorption

https://doi.org/10.1021/acsomega.1c06658
ACS Omega 2022, 7, 7791−7805

energies are almost equal to H_2O. By applying an ortho-fluoro substitution pattern ($F-R_2$) for the SO_2 gas, the difference between H_2O adsorption energy and SO_2 was reduced from −32.7 to −16.8 kJ/mol. This makes H_2O a little less competitive than SO_2. C_2H_4 improved the most under strategy 3. By using a di-ortho fluoro substitution pattern ($F-R_{4,6}$), the difference between H_2O adsorption energy and C_2H_4 gas was reduced from −58.5 to −9.0 kJ/mol. This also makes H_2O less competitive. Strategy 3 is a more balanced approach; it considers the effect functionalization will have on both H_2O and gas adsorption and appeared to be the most effective.

CONCLUSIONS

In this comprehensive study, DFT modeling was carried out to postsynthetically modify STAM-17-OEt linkers with various functional groups to investigate the suitable linker substitution(s) to enhance or moderate gas adsorption and selectivity. The initial benchmark study revealed that the LC-ωPBE density functional with mixed basis sets cc-pVDZ and 6-311G(d,p) was reliable and in good agreement with previous experimental results. Furthermore, it was found that amino- and cyano functionalization led to the most increase in adsorption capabilities. The calculation predicted zwitterionic properties, which provide additional fine-tuning and optimization of the MOF material. Selecting the appropriate functional group and substituted position on the aromatic ring can lead to additional favorable interactions, such as water affinity reduction and switching gas selectivity from one gas to another. Given the initial promising results, this should strongly motivate continued efforts for this strategized functionalization approach. NBO and HOMO−LUMO analyses were performed to help correlate interaction properties to charge distribution and transfer. The results suggest that the MOF exhibits LMCT because of the electron delocalization in the linker and oxidation of the Cu^{2+} cation. Thus, a theoretical post-synthetic modification of the existing STAM-17-OEt materials represents an effective and efficient way to improve the gas capture performance. These efforts are intended to guide the design strategies and advancement of MOFs for gas adsorption and separation applications.

METHODOLOGY

Molecular Cluster Model. Due to the large unit cell of the STAM-17-OEt crystal structure, which contains 1217 atoms, a molecular cluster model strategy was applied where 94 atoms were cut from the bulk material (Figure 10). The cluster model was chosen for this study over a periodic model, where a three-dimensional unit cell is repeated for a full MOF structure representation. This allows for the use of a higher-level electronic structure method and basis set to capture any weak contributions from the different linker substitutions. The molecular cluster model strategy is similar to those in prior studies and they have determined that the choice of the size of a MOF cluster has minimal effect on the adsorption energy and the cluster model is sufficient to describe localized interactions.[37,73,74] The relative adsorption trends over a range of gasses are consistent in periodic and cluster models,[75] as long as the same conditions are applied to all the MOF−gas complex calculations. Because this study considers only the local effect of functionalization on the open-metal site copper, a cluster modeling approach was suitable. The quality of the results is determined mainly by the type of functional, size of the basis set used to describe the atomic orbital, and proper application of dispersion effects, which are considered and described in the next section.

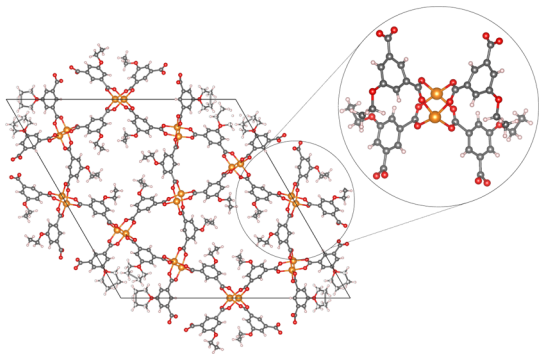

Figure 10. Illustration of the crystal structure of STAM-17-OEt viewed along the *z*-axis, based on the crystallographic information file obtained from the Cambridge Crystallographic Data Center (reference: 1566115).[52] The magnified circle contains the copper paddle-wheel molecular cluster model, composed of two copper atoms, linked by four 5-ethoxy isophthalate linkers. Color key: Cu (gold), O (red), C (gray), and H (off white).

Computational Details. All calculations were performed using the Gaussian 16 package.[76] Geometry optimization of STAM-17-OEt structures and molecular adsorption energy calculations were carried out using the DFT of the Perdew−Burke−Ernzerhof (PBE) exchange−correlation functional.[77] The long-range dispersion corrected version of PBE (LC-ωPBE)[78−80] was used in conjunction with the cc-pVDZ split-valence[81,82] basis set for the Cu atoms and 6-311G(d,p)[83−85] basis set for the remaining atoms. Dunning's correlation consistent basis sets were chosen to correct the basis set superposition error.[82,86,87] The choice of the DFT method and basis set was determined by a comparative study. The accuracy of eight DFT functionals was assessed with respect to experimental enthalpies for CO_2 on $[Cu_3(TMA)_2(H_2O)_3]_n$ MOF or commonly referred to as HKUST-1.[88] LC-ωPBE functional with both cc-pVDZ and 6-311G(d,p) basis sets produce the best results of −14.3 kJ/mol, which is within the range of experimental enthalpy (ΔH_{ads}) of 14.6 ± 0.5−25.6 kJ/mol. LC-ωPBE treated the adsorption carefully and accounted for weak long and medium-range noncovalent forces without overestimation. The bond lengths were comparable to the experimental parameters with an average divergence of 0.01 Å. The full results that include the computed thermodynamic energies and bond lengths compared to published experimental data are reported in the Supporting Information (Table S4 and Figure S4). The same method and basis set was used to calculate the harmonic vibrational frequencies of the optimized geometries to confirm that all local minima were positive frequencies and used to obtain zero-point energy (ZPE) corrections. The self-consistent field parameters used was a tight convergence criterion of 10^{-8} Hartree.

Molecular Cluster Optimization. Geometry optimizations were performed on a truncated molecular cluster cut from an experimentally resolved dehydrated crystal structure of STAM-17-OEt as described in the earlier section. LC-ωPBE with a cc-pVDZ basis set was used for the Cu and 6-311G(d,p) basis set for the other atoms. The cleaved cluster exposed charged carboxylate groups on the linkers, so hydrogen atoms were added to the oxygen atoms to maintain charge neutrality (Figure 11a,b). After the addition of hydrogen atoms to the

https://doi.org/10.1021/acsomega.1c06658
ACS Omega 2022, 7, 7791−7805

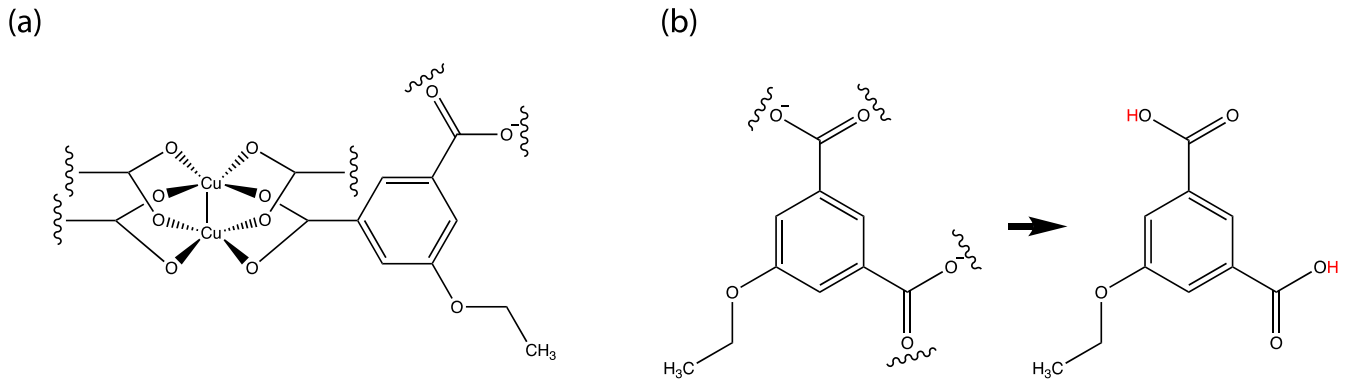

Figure 11. (a) Chemical structure of the molecular cluster model. The wiggle lines denote where atoms are coordinated to the Cu. (b) Chemical structure of the 5-ethoxy isophthalate linker. Hydrogen atoms are added to the exposed charged carboxylate groups.

carboxylate groups, the hydrogens were optimized while keeping the rest of the structure fixed. All STAM-17-OEt models were optimized using the spin-restricted singlet state (S = 0). Cu−dimer complexes are known to have antiferromagnetic and ferromagnetic behaviors;[89] however, the singlet-triplet gap is small[90,91] and adsorption is not dependent on the spin state of Cu.[92] The optimized structure was then functionalized as described in the next section.

Linker Functionalization and Optimization. The optimized STAM-17-OEt molecular clusters were functionalized by replacing the hydrogen atoms of the aromatic ring with the functional groups of interest. Figure 12 illustrates the general scheme used to functionalize the MOF. The chemical modifications were achieved by introducing polar/strong electron-donating groups (EDG) (−NH_2 and −OH), non-polar EDG (−CH_3), polar/strong electron-withdrawing groups (EWG) (−CN and −COOH), and non-polar EWG (F halogen), as well as the number of substituents. For clarity, we use R to denote the different chemical groups introduced into the linkers (R = NH_2, OH, CH_3, CN, COOH, and F). R with a subscript indicates the position (ortho, para) and/or the number of substitutions (mono-, di-, tri-). For example, ortho substitution is represented as (R_2, R_6), di-ortho substitution is represented as ($R_{2,6}$ and $R_{4,6}$), and tri substitution is represented as ($R_{2,4,6}$). R_4 and $R_{2,4}$ were not considered because they have similar chemical environments as R_6 and $R_{2,6}$, respectively. The newly functionalized structure was partially re-optimized; the R groups were optimized while the rest of the structure was fixed.

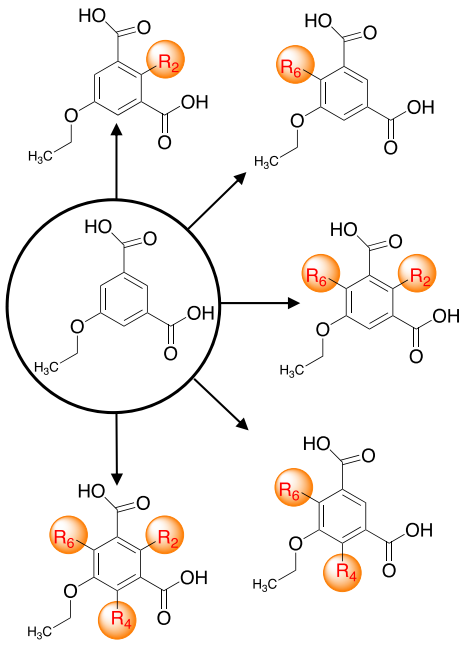

Figure 12. General scheme used to functionalize STAM-17-OEt, showing the positions and number of substituents for different functional groups. Appearing clockwise are ortho substitution R_2 and R_6; di-ortho substitution $R_{2,6}$ and $R_{4,6}$; tri substitution $R_{2,4,6}$. To improve the gas adsorption of the MOF, this strategy was undertaken to modify the linker at various positions.

Adsorption Energies and Thermodynamic Properties. For the adsorption of a gas on STAM-17-OEt calculations, two optimized gas molecules were placed directly above the center of mass of each of the Cu atoms (Figure 13).

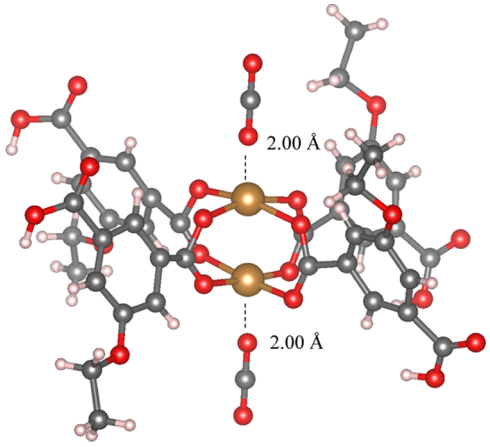

Figure 13. Model used for the DFT STAM-17-OEt and gas adsorption calculations. All gas molecules had a starting geometry of 2.0 Å from the Cu surface.

Two gas molecules were used to retain the MOF's rigidity and prevent distortion during optimization. In a test calculation, where a single CO_2 gas molecule was absorbed on only one side of the copper wheel, the difference in energy was not significant, but it deformed the MOF structure too much in one direction (Table S5), presumably due to the Jahn−Teller distortion.[93] The apical Cu−O bonds are longer than Cu−O bonds in the basal plane. The DFT calculations reveal that the Jahn−Teller distortions are enhanced upon CO_2 gas adsorption and apical bond elongation is observed. The e_g

https://doi.org/10.1021/acsomega.1c06658
ACS Omega 2022, 7, 7791−7805

orbitals involved in the degeneracy point toward the CO_2 molecule, so the distortion results in energetic stabilization. These observations are consistent with an earlier study.[73]

Furthermore, the effect of the distortion on the Cu^{2+} coordination environment provides unique properties. The adsorption capability of MOFs depends on the availability of the metal site. Cu^{2+} ions, which exhibit a Jahn−Teller distortion, have fully desorbed and exposed metal sites which increase adsorption potential and gas selectivity.[94]

During the optimization, Cu−Cu and the gas molecule were free to move, while the remaining structure was constrained. This allows for the structural transformations that occur during adsorption,[95−97] while minimizing computational cost. The geometry optimization strategy was validated by comparing a fully optimized MOF−gas complex without restrictions (CO, CO_2, and H_2O) to the partially optimized structure, where only the Cu atoms and gas molecules were free to move. The differences in the adsorption energies of the fully optimized structures compared to the partially optimized structures are small, −3.0, −3.0, and −2.4 kJ/mol, respectively. The relative adsorption energy trends of the fully and partially optimized are consistent, $H_2O > CO_2 > CO$ (Table S6).

The optimized geometry of the adsorbate−cluster complex was confirmed to be a true minimum by vibrational frequency calculations. Adsorption energy (ΔE_{ads}) per adsorbate gas molecule was computed via:

$$\Delta E_{ads} = \frac{1}{2}(E_{2gas\_MOF} - 2E_{gas} - E_{MOF}) \quad (1)$$

where E_{MOF} is the energy of the bare MOF, E_{gas} is the energy of the gas molecule, and E_{MOF} is the energy of the gas molecule adsorbed on the MOF. Because there are two adsorbents on either side of the Cu atom, the total energy is obtained by dividing by two.

For reference, other thermodynamic properties were also computed. ΔH_{ads} at 298 K is

$$\Delta H_{ads}(298) = \frac{1}{2}(\Delta E_{ads}(0\ K) + 2\Delta ZPE + 2\Delta Th_H) \quad (2)$$

Analogous to the enthalpy, ΔE_{ads} at 298 K can be found from

$$\Delta E_{ads}(298) = \frac{1}{2}(\Delta E_{ads}(0\ K) + 2\Delta ZPE + 2\Delta Th_E) \quad (3)$$

where ΔE_{ads}, ΔZPE, and ΔTh_E are the sum of the electronic energy, zero-point vibrational energy, and thermal correction to the internal energy at 298 K, respectively. With these definitions, atomic heats of formation at 0 K can be converted to those at 298 K.

Charge Distribution Analysis. Natural bond orbital (NBO) analysis was performed to gain more insights into the stabilization and charge delocalization of the electron density, which can enhance the understanding of intra-/intermolecular interactions that occur during adsorption. To calculate the second-order interactions between the filled and unfilled orbitals, NBO calculations were performed using NBO version 3.1,[98−105] as implemented in the Gaussian 16 package[76] with LC-ωPBE and basis sets described in the earlier sections. This long-range-corrected DFT satisfies Koopman's theorem and accurately calculates orbital energies and HOMO−LUMO energy gaps for molecular systems.[106] Alternative orbital localization algorithms, the Mulliken[107] population analysis, and Pipek-Mezey[108] localization criteria, using Gaussian keyword IOp(4/9=20212), were also implemented. Visualization for Electronic and Structural Analysis (VESTA)[109] software was used to generate the orbital visualizations.

■ ASSOCIATED CONTENT

Supporting Information

The Supporting Information is available free of charge at https://pubs.acs.org/doi/10.1021/acsomega.1c06658.

DFT raw data output files containing optimized geometries of the 681 unmodified and functionalized STAM-17-OEt MOF structures and STAM-17-OEt + gas complexes[63] (PDF)

■ AUTHOR INFORMATION

Corresponding Author

Uchenna A. Anene − *Department of Chemical and Biomolecular Engineering, University of Connecticut, Storrs, Connecticut 06269, United States;* orcid.org/0000-0003-4162-5122; Email: uchenna.anene@uconn.edu

Author

S. Pamir Alpay − *Department of Materials Science and Engineering, Institute of Materials Science and Department of Physics, University of Connecticut, Storrs, Connecticut 06269, United States;* orcid.org/0000-0003-4480-1558

Complete contact information is available at: https://pubs.acs.org/10.1021/acsomega.1c06658

Author Contributions

The computational study was designed and carried out by U.A.A. The manuscript was written by U.A.A and revised by S.P.A.

Notes

The authors declare no competing financial interest.

■ ACKNOWLEDGMENTS

This research was supported in part through computational resources provided by the University of Connecticut High-Performance Computing facility. U.A.A. is immensely thankful to Professor Nikita Matsunaga (Long Island University, Brooklyn, NY) and Jean-Paul Bourgault, Ph.D. for their insightful comments and discussions and Kingsley Chukwu, Ph.D. for always being available to help troubleshoot codes. U.A.A. also thanks Gemechis Degaga, Ph.D. for introducing her to the MOF world.

■ REFERENCES

(1) Peplow, M. Materials science: The hole story. *Nature* **2015**, *520*, 148−150.

(2) BASF metal organic frameworks (MOFs): innovative fuel systems for natural gas vehicles (NGVs). *Chem. Soc. Rev.* **2014**, *43*, 6173−6174. DOI: 10.1039/C4CS90070G

(3) Frameworks for commercial success. *Nat. Chem.* **2016**, *8*, 987. DOI: 10.1038/nchem.2661

(4) Arno, J.; Farha, O.; Morris, W.; Siu, P.; Tom, G.; Weston, M.; Fuller, P.; McCabe, J.; Ameen, M. A new class of adsorbent materials offer high capacity storage and safe delivery of dopant gases. https://www.numat.tech/ion-x-oem-data (accessed Sep 7, 2018).

(5) Arnó, J.; Farha, O. K.; Morris, W.; Siu, P. W.; Tom, G. M.; Weston, M. H.; Fuller, P. E. ION-X dopant gas delivery system performance characterization at axcelis, *2018 22nd International*

Conference on Ion Implantation Technology (IIT), 16−21 Sep 2018; 2018; pp 227−230.
(6) Clark, J. Mercedes-Benz F125! research vehicle technology. https://emercedesbenz.com/autos/mercedes-benz/concept-vehicles/mercedes-benz-f125-research-vehicle-technology/ (accessed Aug 3, 2011).
(7) Zhu, L.; Liu, X.-Q.; Jiang, H.-L.; Sun, L.-B. Metal-organic frameworks for heterogeneous basic catalysis. *Chem. Rev.* **2017**, *117*, 8129−8176.
(8) Wu, Y.; Li, Y.; Gao, J.; Zhang, Q. Recent advances in vacancy engineering of metal-organic frameworks and their derivatives for electrocatalysis. *SusMat* **2021**, *1*, 66−87.
(9) Wu, M.-X.; Yang, Y.-W. Metal-organic framework (MOF)-based drug/cargo delivery and cancer therapy. *Adv. Mater.* **2017**, *29*, 1606134.
(10) Crivello, C.; Sevim, S.; Graniel, O.; Franco, C.; Pané, S.; Puigmartí-Luis, J.; Muñoz-Rojas, D. Advanced technologies for the fabrication of MOF thin films. *Mater. Horiz.* **2021**, *8*, 168−178.
(11) Zhu, J. P.; Wang, X. H.; Zuo, X. X. The application of metal-organic frameworks in electrode materials for lithium−ion and lithium−sulfur batteries. *R. Soc. Open Sci.* **2019**, *6*, 190634.
(12) Wu, Z.; Xie, J.; Xu, Z. J.; Zhang, S.; Zhang, Q. Recent progress in metal−organic polymers as promising electrodes for lithium/sodium rechargeable batteries. *J. Mater. Chem. A* **2019**, *7*, 4259−4290.
(13) Li, H.; Eddaoudi, M.; O'Keeffe, M.; Yaghi, O. M. Design and synthesis of an exceptionally stable and highly porous metal-organic framework. *Nature* **1999**, *402*, 276−279.
(14) Liu, J.; Thallapally, P. K.; Strachan, D. Metal-Organic frameworks for removal of Xe and Kr from nuclear fuel reprocessing plants. *Langmuir* **2012**, *28*, 11584−11589.
(15) Peralta, D.; Chaplais, G.; Simon-Masseron, A.; Barthelet, K.; Chizallet, C.; Quoineaud, A.-A.; Pirngruber, G. D. Comparison of the behavior of metal−organic frameworks and zeolites for hydrocarbon separations. *J. Am. Chem. Soc.* **2012**, *134*, 8115−8126.
(16) Blay, V.; Bobadilla, L. F.; García, A. C. *Zeolites and Metal−Organic Frameworks*; Ngô, C., Ed.; Amsterdam University Press, 2018.
(17) Jin, H.; Wollbrink, A.; Yao, R.; Li, Y.; Caro, J.; Yang, W. A novel CAU-10-H MOF membrane for hydrogen separation under hydrothermal conditions. *J. Membr. Sci.* **2016**, *513*, 40−46.
(18) Zu, K.; Cui, S.; Qin, M. Performance comparison between metal-organic framework (MOFs) and conventional desiccants (silica gel, zeolite) for a novel high temperature cooling system. *IOP Conf. Ser.: Mater. Sci. Eng.* **2019**, *609*, 052013.
(19) Horowitz, C. A. Paris Agreement. *Int. Leg. Mater.* **2016**, *55*, 740−755.
(20) Thakur, I. S.; Kumar, M.; Varjani, S. J.; Wu, Y.; Gnansounou, E.; Ravindran, S. Sequestration and utilization of carbon dioxide by chemical and biological methods for biofuels and biomaterials by chemoautotrophs: Opportunities and challenges. *Bioresour. Technol.* **2018**, *256*, 478−490.
(21) De Silva, G. P. D.; Ranjith, P. G.; Perera, M. S. A. Geochemical aspects of CO2 sequestration in deep saline aquifers: A review. *Fuel* **2015**, *155*, 128−143.
(22) Cheah, W. Y.; Ling, T. C.; Juan, J. C.; Lee, D.-J.; Chang, J.-S.; Show, P. L. Biorefineries of carbon dioxide: from carbon capture and storage (CCS) to bioenergies production. *Bioresour. Technol.* **2016**, *215*, 346−356.
(23) Zhang, Z.; Wang, H.; Chen, D.; Li, Q.; Thai, P.; Gong, D.; Li, Y.; Zhang, C.; Gu, Y.; Zhou, L.; Morawska, L.; Wang, B. Emission characteristics of volatile organic compounds and their secondary organic aerosol formation potentials from a petroleum refinery in Pearl River Delta, China. *Sci. Total Environ.* **2017**, *584−585*, 1162−1174.
(24) Amoatey, P.; Omidvarborna, H.; Baawain, M. S.; Al-Mamun, A. Emissions and exposure assessments of SOX, NOX, PM10/2.5 and trace metals from oil industries: A review study (2000−2018). *Process Saf. Environ. Prot.* **2019**, *123*, 215−228.
(25) Amoatey, P.; Omidvarborna, H.; Affum, H. A.; Baawain, M. Performance of AERMOD and CALPUFF models on SO2 and NO2 emissions for future health risk assessment in Tema Metropolis. *Hum. Ecol. Risk Assess.* **2019**, *25*, 772−786.
(26) Torrisi, A.; Bell, R. G.; Mellot-Draznieks, C. Predicting the impact of functionalized ligands on CO2 adsorption in MOFs: A combined DFT and Grand Canonical Monte Carlo study. *Microporous Mesoporous Mater.* **2013**, *168*, 225−238.
(27) Kumar, P.; Kim, K.-H.; Kwon, E. E.; Szulejko, J. E. Metal organic frameworks for the control and management of air quality: advances and future direction. *J. Mater. Chem.* **2016**, *4*, 345−361.
(28) Kang, Z.; Fan, L.; Sun, D. Recent advances and challenges of metal−organic framework membranes for gas separation. *J. Mater. Chem. A* **2017**, *5*, 10073−10091.
(29) Wang, H.; Lustig, W. P.; Li, J. Sensing and capture of toxic and hazardous gases and vapors by metal−organic frameworks. *Chem. Soc. Rev.* **2018**, *47*, 4729−4756.
(30) Suh, M. P.; Park, H. J.; Prasad, T. K.; Lim, D.-W. Hydrogen storage in metal−organic frameworks. *Chem. Rev.* **2012**, *112*, 782−835.
(31) Kapelewski, M. T.; Runčevski, T.; Tarver, J. D.; Jiang, H. Z. H.; Hurst, K. E.; Parilla, P. A.; Ayala, A.; Gennett, T.; FitzGerald, S. A.; Brown, C. M.; Long, J. R. Record high hydrogen storage capacity in the metal−organic framework Ni2(m-dobdc) at near-ambient temperatures. *Chem. Mater.* **2018**, *30*, 8179−8189.
(32) Li, H.; Wang, K.; Sun, Y.; Lollar, C. T.; Li, J.; Zhou, H.-C. Recent advances in gas storage and separation using metal−organic frameworks. *Mater. Today* **2018**, *21*, 108−121.
(33) Wang, Z.; Cohen, S. M. Postsynthetic covalent modification of a neutral metal-organic framework. *J. Am. Chem. Soc.* **2007**, *129*, 12368−12369.
(34) Mandal, S.; Natarajan, S.; Mani, P.; Pankajakshan, A. Post-synthetic modification of metal-organic frameworks toward applications. *Adv. Funct. Mater.* **2021**, *31*, 2006291.
(35) Wang, Z.; Cohen, S. M. Postsynthetic modification of metal−organic frameworks. *Chem. Soc. Rev.* **2009**, *38*, 1315−1329.
(36) Kalaj, M.; Cohen, S. M. Postsynthetic modification: an enabling technology for the advancement of metal-organic frameworks. *ACS Cent. Sci.* **2020**, *6*, 1046−1057.
(37) Bernales, V.; Ortuño, M. A.; Truhlar, D. G.; Cramer, C. J.; Gagliardi, L. Computational design of functionalized metal−organic framework nodes for catalysis. *ACS Cent. Sci.* **2018**, *4*, 5−19.
(38) Li, Y.; Fu, Y.; Ni, B.; Ding, K.; Chen, W.; Wu, K.; Huang, X.; Zhang, Y. Effects of ligand functionalization on the photocatalytic properties of titanium-based MOF: A density functional theory study. *AIP Adv.* **2018**, *8*, 035012.
(39) You, W.; Liu, Y.; Howe, J. D.; Tang, D.; Sholl, D. S. Tuning binding tendencies of small molecules in metal−organic frameworks with open metal sites by metal substitution and linker functionalization. *J. Phys. Chem. C* **2018**, *122*, 27486−27494.
(40) Lee, K.; Howe, J. D.; Lin, L.-C.; Smit, B.; Neaton, J. B. Small-molecule adsorption in open-site metal-organic frameworks: a systematic density functional theory study for rational design. *Chem. Mater.* **2015**, *27*, 668−678.
(41) Ding, M.; Cai, X.; Jiang, H.-L. Improving MOF stability: approaches and applications. *Chem. Sci.* **2019**, *10*, 10209−10230.
(42) Zhou, H.-C.; Long, J. R.; Yaghi, O. M. Introduction to metal−organic frameworks. *Chem. Rev.* **2012**, *112*, 673−674.
(43) Sosa, J.; Bennett, T.; Nelms, K.; Liu, B.; Tovar, R.; Liu, Y. Metal−organic framework hybrid materials and their applications. *Crystals* **2018**, *8*, 325.
(44) Long, J. R.; Yaghi, O. M. The pervasive chemistry of metal−organic frameworks. *Chem. Soc. Rev.* **2009**, *38*, 1213−1214.
(45) Mai, Z.; Liu, D. Synthesis and applications of isoreticular metal-organic frameworks IRMOFs-n (n = 1, 3, 6, 8). *Cryst. Growth Des.* **2019**, *19*, 7439−7462.
(46) Bosch, M.; Zhang, M.; Zhou, H.-C. Increasing the stability of metal-organic frameworks. *Adv. Chem.* **2014**, *2014*, 182327.
(47) Rosi, N. L.; Eddaoudi, M.; Kim, J.; O'Keeffe, M.; Yaghi, O. M. Infinite secondary building units and forbidden catenation in metal-organic frameworks. *Angew. Chem., Int. Ed.* **2002**, *41*, 284−287.

https://doi.org/10.1021/acsomega.1c06658
ACS Omega 2022, 7, 7791−7805

(48) McHugh, L. N.; McPherson, M. J.; McCormick, L. J.; Morris, S. A.; Wheatley, P. S.; Teat, S. J.; McKay, D.; Dawson, D. M.; Sansome, C. E. F.; Ashbrook, S. E.; Stone, C. A.; Smith, M. W.; Morris, R. E. Hydrolytic stability in hemilabile metal−organic frameworks. *Nat. Chem.* **2018**, *10*, 1096−1102.
(49) Yang, Q.; Zhong, C. Understanding hydrogen adsorption in metal-organic frameworks with open metal sites:a computational study. *J. Phys. Chem. B* **2006**, *110*, 655−658.
(50) Chen, B.; Ockwig, N. W.; Millward, A. R.; Contreras, D. S.; Yaghi, O. M. High H2 adsorption in a microporous metal-organic framework with open metal sites. *Angew. Chem., Int. Ed.* **2005**, *44*, 4745−4749.
(51) Chen, B.; Eddaoudi, M.; Reineke, T. M.; Kampf, J. W.; O'Keeffe, M.; Yaghi, O. M. Cu2(ATC)·6H2O:designof open metal sites in porous metal−organic crystals (ATC:1, 3,5,7-adamantanetetracarboxylate). *J. Am. Chem. Soc.* **2000**, *122*, 11559−11560.
(52) McHugh, L. N.; McCormick, L. J.; Morris, S. A.; Wheatley, P. S.; David McKay, S. J. T.; Dawson, D. M.; Sansome, C. E. F.; Ashbrook, S. E.; Stone, C. A.; Smith, M. W.; Morris, R. E. *CCDC 1566115: Experimental Crystal Structure Determination*, 2018.
(53) Peterson, G. W.; Wagner, G. W.; Balboa, A.; Mahle, J.; Sewell, T.; Karwacki, C. J. Ammonia vapor removal by Cu3(BTC)2 and its characterization by MAS NMR. *J. Phys. Chem. C* **2009**, *113*, 13906−13917.
(54) McHugh, L. N.; Terracina, A.; Wheatley, P. S.; Buscarino, G.; Smith, M. W.; Morris, R. E. Metal-organic framework-activated carbon composite materials for the removal of ammonia from contaminated airstreams. *Angew. Chem., Int. Ed.* **2019**, *58*, 11747−11751.
(55) Terracina, A.; McHugh, L. N.; Mazaj, M.; Vrtovec, N.; Agnello, S.; Cannas, M.; Gelardi, F. M.; Morris, R. E.; Buscarino, G. Structure effects induced by high mechanical compaction of STAM-17-OEt MOF powders. *Eur. J. Inorg. Chem.* **2021**, *2021*, 2334−2342.
(56) Christmann, K. *Introduction to Surface Physical Chemistry*, 1st ed.; Baumgärtel, H., Franck, E. U., Grünbein, W., Eds.; Steinkopff, Heidelberg, 1991; pp 51−52.
(57) Zlotea, C.; Phanon, D.; Mazaj, M.; Heurtaux, D.; Guillerm, V.; Serre, C.; Horcajada, P.; Devic, T.; Magnier, E.; Cuevas, F.; Férey, G.; Llewellyn, P. L.; Latroche, M. Effect of NH2 and CF3 functionalization on the hydrogen sorption properties of MOFs. *Dalton Trans.* **2011**, *40*, 4879−4881.
(58) Su, Z.; Chen, J. H.; Sun, X.; Huang, Y.; Dong, X. Amine-functionalized metal organic framework (NH2-MIL-125(Ti)) incorporated sodium alginate mixed matrix membranes for dehydration of acetic acid by pervaporation. *RSC Adv.* **2015**, *5*, 99008−99017.
(59) Islamoglu, T.; Ortuño, M. A.; Proussaloglou, E.; Howarth, A. J.; Vermeulen, N. A.; Atilgan, A.; Asiri, A. M.; Cramer, C. J.; Farha, O. K. Presence versus proximity: the role of pendant amines in the catalytic hydrolysis of a nerve agent simulant. *Angew. Chem., Int. Ed.* **2018**, *57*, 1949−1953.
(60) Karmakar, A.; Desai, A. V.; Ghosh, S. K. Ionic metal-organic frameworks (iMOFs): design principles and applications. *Coord. Chem. Rev.* **2016**, *307*, 313−341.
(61) Petit, C.; Levasseur, B.; Mendoza, B.; Bandosz, T. J. Reactive adsorption of acidic gases on MOF/graphite oxide composites. *Microporous Mesoporous Mater.* **2012**, *154*, 107−112.
(62) Levasseur, B.; Petit, C.; Bandosz, T. J. Reactive adsorption of NO2 on copper-based metal−organic framework and graphite oxide/metal−organic framework composites. *ACS Appl. Mater. Interfaces* **2010**, *2*, 3606−3613.
(63) Anene, U. A.; Alpay, S. P. STAM-17-OEt metal-organic frameworks (MOF) dataset: results of DFT LC-ωPBE/cc-pVDZ, 6-311G(dp) geometry optimizations of unmodified and functionalized MOFs. *NoMaD Repository*, 2021.
(64) Férey, G.; Serre, C. Large breathing effects in three-dimensional porous hybrid matter: facts, analyses, rules and consequences. *Chem. Soc. Rev.* **2009**, *38*, 1380−1399.
(65) Loiseau, T.; Serre, C.; Huguenard, C.; Fink, G.; Taulelle, F.; Henry, M.; Bataille, T.; Férey, G. A rationale for the large breathing of the porous aluminum terephthalate (MIL-53) upon hydration. *Chem.—Eur. J.* **2004**, *10*, 1373−1382.
(66) Alhamami, M.; Doan, H.; Cheng, C.-H. Review on breathing behaviors of metal-organic-frameworks (MOFs) for gas adsorption. *Materials* **2014**, *7*, 3198−3250.
(67) Li, C.; Wang, K.; Li, J.; Zhang, Q. Recent progress in stimulus-responsive two-mimensional metal-organic frameworks. *ACS Mater. Lett.* **2020**, *2*, 779−797.
(68) Koo, W.-T.; Yu, S.; Choi, S.-J.; Jang, J.-S.; Cheong, J. Y.; Kim, I.-D. Nanoscale PdO catalyst functionalized Co3O4 hollow nanocages using MOF templates for selective detection of acetone molecules in exhaled breath. *ACS Appl. Mater. Interfaces* **2017**, *9*, 8201−8210.
(69) Koo, W.-T.; Jang, J.-S.; Kim, I.-D. Metal-organic frameworks for chemiresistive sensors. *Chem* **2019**, *5*, 1938−1963.
(70) Ling, S.; Slater, B. Unusually large band gap changes in breathing metal−organic framework material. *J. Phys. Chem. C* **2015**, *119*, 16667−16677.
(71) Berger, A. H.; Bhown, A. S. Comparing physisorption and chemisorption solid sorbents for use separating CO2 from flue gas using temperature swing adsorption. *Energy Procedia* **2011**, *4*, 562−567.
(72) Wang, J.; Huang, L.; Yang, R.; Zhang, Z.; Wu, J.; Gao, Y.; Wang, Q.; O'Hare, D.; Zhong, Z. Recent advances in solid sorbents for CO2 capture and new development trends. *Energy Environ. Sci.* **2014**, *7*, 3478−3518.
(73) Fischer, M.; Gomes, J. R. B.; Fröba, M.; Jorge, M. Modeling adsorption in metal-organic frameworks with open metal sites: propane/propylene separations. *Langmuir* **2012**, *28*, 8537−8549.
(74) Li, Z.; Peters, A. W.; Bernales, V.; Ortuño, M. A.; Schweitzer, N. M.; DeStefano, M. R.; Gallington, L. C.; Platero-Prats, A. E.; Chapman, K. W.; Cramer, C. J.; Gagliardi, L.; Hupp, J. T.; Farha, O. K. Metal−organic framework supported cobalt catalysts for the oxidative dehydrogenation of propane at low temperature. *ACS Cent. Sci.* **2017**, *3*, 31−38.
(75) Lee, K.; Isley, W. C.; Dzubak, A. L.; Verma, P.; Stoneburner, S. J.; Lin, L.-C.; Howe, J. D.; Bloch, E. D.; Reed, D. A.; Hudson, M. R.; Brown, C. M.; Long, J. R.; Neaton, J. B.; Smit, B.; Cramer, C. J.; Truhlar, D. G.; Gagliardi, L. Design of a metal−organic framework with enhanced back bonding for separation of N2 and CH4. *J. Am. Chem. Soc.* **2014**, *136*, 698−704.
(76) Frisch, M. J.; Trucks, G. W.; Schlegel, H. B.; Scuseria, G. E.; Robb, M. A.; Cheeseman, J. R.; Scalmani, G.; Barone, V.; Petersson, G. A.; Nakatsuji, H.; Li, X.; Caricato, M.; Marenich, A. V.; Bloino, J.; Janesko, B. G.; Gomperts, R.; Mennucci, B.; Hratchian, H. P.; Ortiz, J. V.; Izmaylov, A. F.; Sonnenberg, J. L.; Williams; Ding, F.; Lipparini, F.; Egidi, F.; Goings, J.; Peng, B.; Petrone, A.; Henderson, T.; Ranasinghe, D.; Zakrzewski, V. G.; Gao, J.; Rega, N.; Zheng, G.; Liang, W.; Hada, M.; Ehara, M.; Toyota, K.; Fukuda, R.; Hasegawa, J.; Ishida, M.; Nakajima, T.; Honda, Y.; Kitao, O.; Nakai, H.; Vreven, T.; Throssell, K.; Montgomery, J. A., Jr.; Peralta, J. E.; Ogliaro, F.; Bearpark, M. J.; Heyd, J. J.; Brothers, E. N.; Kudin, K. N.; Staroverov, V. N.; Keith, T. A.; Kobayashi, R.; Normand, J.; Raghavachari, K.; Rendell, A. P.; Burant, J. C.; Iyengar, S. S.; Tomasi, J.; Cossi, M.; Millam, J. M.; Klene, M.; Adamo, C.; Cammi, R.; Ochterski, J. W.; Martin, R. L.; Morokuma, K.; Farkas, O.; Foresman, J. B.; Fox, D. J. *Gaussian 16* Rev. C.01, Wallingford, CT, 2016.
(77) Perdew, J. P.; Burke, K.; Ernzerhof, M. Generalized gradient approximation made simple. *Phys. Rev. Lett.* **1996**, *77*, 3865−3868.
(78) Vydrov, O. A.; Scuseria, G. E. Assessment of a long-range corrected hybrid functional. *J. Chem. Phys.* **2006**, *125*, 234109.
(79) Vreven, T.; Frisch, M. J.; Kudin, K. N.; Schlegel, H. B.; Morokuma, K. Geometry optimization with QM/MM methods II: Explicit quadratic coupling. *Mol. Phys.* **2006**, *104*, 701−714.
(80) Vydrov, O. A.; Scuseria, G. E.; Perdew, J. P. Tests of functionals for systems with fractional electron number. *J. Chem. Phys.* **2007**, *126*, 154109.
(81) Balabanov, N. B.; Peterson, K. A. Basis set limit electronic excitation energies, ionization potentials, and electron affinities for the

https://doi.org/10.1021/acsomega.1c06658
ACS Omega 2022, 7, 7791−7805

3d transition metal atoms: Coupled cluster and multireference methods. *J. Chem. Phys.* **2006**, *125*, 074110.
(82) Dunning, T. H. Gaussian basis sets for use in correlated molecular calculations. I. The atoms boron through neon and hydrogen. *J. Chem. Phys.* **1989**, *90*, 1007−1023.
(83) Binning, R. C., Jr; Curtiss, L. A. Compact contracted basis sets for third-row atoms: Ga−Kr. *J. Comput. Chem.* **1990**, *11*, 1206−1216.
(84) McGrath, M. P.; Radom, L. Extension of Gaussian-1 (G1) theory to bromine-containing molecules. *J. Chem. Phys.* **1991**, *94*, 511−516.
(85) Curtiss, L. A.; McGrath, M. P.; Blaudeau, J. P.; Davis, N. E.; Binning, R. C.; Radom, L. Extension of Gaussian-2 theory to molecules containing third-row atoms Ga−Kr. *J. Chem. Phys.* **1995**, *103*, 6104−6113.
(86) Fischer, M.; Gomes, J. R. B.; Jorge, M. Computational approaches to study adsorption in MOFs with unsaturated metal sites. *Mol. Simul.* **2014**, *40*, 537−556.
(87) Kendall, R. A.; Dunning, T. H.; Harrison, R. J. Electron affinities of the first-row atoms revisited. Systematic basis sets and wave functions. *J. Chem. Phys.* **1992**, *96*, 6796−6806.
(88) Chui, S. S.-Y.; Lo, S. M.-F.; Charmant, J. P. H.; Orpen, A. G.; Williams, I. D. A chemically functionalizable nanoporous material [Cu3(TMA)2(H2O)3]n. *Science* **1999**, *283*, 1148.
(89) Bleaney, B. Anomalous paramagnetism of copper acetate. *Rev. Mod. Phys.* **1953**, *25*, 161−162.
(90) de Loth, P.; Daudey, J. P.; Astheimer, H.; Walz, L.; Haase, W. Direct theoretical ab initio calculations in exchange coupled copper(II) dimers: Influence of the choice of the atomic basis set on the singlet−triplet splitting in modeled and real copper dimers. *J. Chem. Phys.* **1985**, *82*, 5048−5052.
(91) De Loth, P.; Cassoux, P.; Daudey, J. P.; Malrieu, J. P. Ab initio direct calculation of the singlet-triplet separation in cupric acetate hydrate dimer. *J. Am. Chem. Soc.* **1981**, *103*, 4007−4016.
(92) Grajciar, L.; Bludský, O.; Nachtigall, P. Water adsorption on coordinatively unsaturated sites in CuBTC MOF. *J. Phys. Chem. Lett.* **2010**, *1*, 3354−3359.
(93) Jahn, H. A.; Teller, E.; Donnan, F. G. Stability of polyatomic molecules in degenerate electronic states I-orbital degeneracy. *Proc. R. Soc. London, Ser. A* **1937**, *161*, 220−235.
(94) Mu, B.; Li, F.; Walton, K. S. A novel metal−organic coordination polymer for selective adsorption of CO2 over CH4. *Chem. Commun.* **2009**, 2493−2495.
(95) Alzahrani, K. A. H.; Deeth, R. J. A computational analysis of the intrinsic plasticity of five-coordinate Cu(II) complexes and the factors leading to the breakdown of the orbital directing effect in paddlewheel secondary building units. *J. Comput. Chem.* **2020**, *41*, 340−348.
(96) Zhou, W.; Wu, H.; Yildirim, T. Enhanced H2 adsorption in isostructural metal−organic frameworks with open metal sites: strong dependence of the binding strength on metal ions. *J. Am. Chem. Soc.* **2008**, *130*, 15268−15269.
(97) Yu, D.; Yazaydin, A. O.; Lane, J. R.; Dietzel, P. D. C.; Snurr, R. Q. A combined experimental and quantum chemical study of CO2 adsorption in the metal−organic framework CPO-27 with different metals. *Chem. Sci.* **2013**, *4*, 3544−3556.
(98) Weinhold, F.; Carpenter, J. E. *The Structure of Small Molecules and Ions*; Naaman, R., Vager, Z., Eds.; Plenum, 1988; pp 227−236.
(99) Reed, A. E.; Weinhold, F. Natural bond orbital analysis of near-Hartree−Fock water dimer. *J. Chem. Phys.* **1983**, *78*, 4066−4073.
(100) Weinhold, F.; Glendening, E. D. Comment on "natural bond orbitals and the nature of the hydrogen bond". *J. Phys. Chem. A* **2018**, *122*, 724−732.
(101) Carpenter, J. E. *Extension of Lewis Structure Concepts to Open-Shell and Excited-State Molecular Species*; University of Wisconsin--Madison, 1987.
(102) Reed, A. E.; Curtiss, L. A.; Weinhold, F. Intermolecular interactions from a natural bond orbital, donor-acceptor viewpoint. *Chem. Rev.* **1988**, *88*, 899−926.
(103) Foster, J. P.; Weinhold, F. Natural hybrid orbitals. *J. Am. Chem. Soc.* **1980**, *102*, 7211−7218.
(104) Reed, A. E.; Weinhold, F. Natural localized molecular orbitals. *J. Chem. Phys.* **1985**, *83*, 1736−1740.
(105) Reed, A. E.; Weinstock, R. B.; Weinhold, F. Natural population analysis. *J. Chem. Phys.* **1985**, *83*, 735−746.
(106) Tsuneda, T.; Song, J.-W.; Suzuki, S.; Hirao, K. On Koopmans' theorem in density functional theory. *J. Chem. Phys.* **2010**, *133*, 174101.
(107) Mulliken, R. S. Electronic population analysis on LCAO−MO molecular wave functions. I. *J. Chem. Phys.* **1955**, *23*, 1833−1840.
(108) Pipek, J.; Mezey, P. G. A fast intrinsic localization procedure applicable for ab initio and semiempirical linear combination of atomic orbital wave functions. *J. Chem. Phys.* **1989**, *90*, 4916−4926.
(109) Momma, K.; Izumi, F. VESTA 3 for three-dimensional visualization of crystal, volumetric and morphology data. *J. Appl. Crystallogr.* **2011**, *44*, 1272−1276.

https://doi.org/10.1021/acsomega.1c06658
ACS Omega 2022, 7, 7791−7805